Calving of a large Greenlandic tidewater glacier has complex links to meltwater plumes and mélange

Samuel Cook[1], Poul Christoffersen[2], Martin Truffer[3], Thomas Russell Chudley[1], and Antonio Abellan[4]

[1]Scott Polar Research Institute
[2]University of Cambridge
[3]University of Alaska Fairbanks
[4]Institute of Applied Geosciences, University of Leeds

November 24, 2022

Abstract

Calving and solid ice discharge into fjords account for approximately half of the annual net ice loss from the Greenland Ice Sheet, but these processes are rarely observed. To gain insights into the spatio-temporal nature of calving, we use a terrestrial radar interferometer to derive a three-week record of 8,026 calving events from Store Glacier, including the transition between a mélange-filled and ice-free fjord. We show that calving rates double across this transition and that the interferometer record is in good agreement with volumetric estimates of calving losses from contemporaneous UAV surveys. We report significant variations in calving activity over time, which obfuscate any simple power-law relationship. While there is a statistically significant relationship between surface melt and the number of calving events, no such relationship exists between surface melt and the volume of these events. Similarly, we find a 70% increase in the number of calving events in the presence of visible meltwater plumes, but only a 3% increase in calving volumes. While calving losses appear to have no clear single control, we find a bimodal distribution of iceberg sizes due to small sections of ice breaking off the subaerial part of the front and large capsizing icebergs forming by full-thickness failure. Whereas previous work has hypothesised that tidewater glaciers can be grouped according to whether they calve predominantly by the former or latter mechanism, our observations indicate that calving here inherently comprises both, and that the dominant process can change over relatively short periods.

1

Calving of a large Greenlandic tidewater glacier has complex links to meltwater plumes and mélange

Samuel J. Cook[1][†], Poul Christoffersen[1], Martin Truffer[2], Thomas R. Chudley[1], Antonio Abellán[3].

[†]Corresponding Author (sc690@cam.ac.uk)
[1]Scott Polar Research Institute, University of Cambridge
[2]Geophysical Institute, University of Alaska, Fairbanks, USA
[3]Institute of Applied Geosciences, School of Earth and Environment, University of Leeds

Key Points:

- We derive a record of 8,026 calving events at Store Glacier in July 2017 using a terrestrial radar interferometer

- We find no single clear control on calving and clear variations in calving behaviour over time, producing a bimodal calving distribution

- Our findings suggest that grouping glaciers by their dominant calving mechanism is not tenable, as this mechanism can change over time

16 **Abstract**

17 Calving and solid ice discharge into fjords account for approximately half of the annual net ice
18 loss from the Greenland Ice Sheet, but these processes are rarely observed. To gain insights into
19 the spatio-temporal nature of calving, we use a terrestrial radar interferometer to derive a three-
20 week record of 8,026 calving events from Store Glacier, including the transition between a
21 mélange-filled and ice-free fjord. We show that calving rates double across this transition and
22 that the interferometer record is in good agreement with volumetric estimates of calving losses
23 from contemporaneous UAV surveys. We report significant variations in calving activity over
24 time, which obfuscate any simple power-law relationship. While there is a statistically significant
25 relationship between surface melt and the number of calving events, no such relationship exists
26 between surface melt and the volume of these events. Similarly, we find a 70% increase in the
27 number of calving events in the presence of visible meltwater plumes, but only a 3% increase in
28 calving volumes. While calving losses appear to have no clear single control, we find a bimodal
29 distribution of iceberg sizes due to small sections of ice breaking off the subaerial part of the
30 front and large capsizing icebergs forming by full-thickness failure. Whereas previous work has
31 hypothesised that tidewater glaciers can be grouped according to whether they calve
32 predominantly by the former or latter mechanism, our observations indicate that calving here
33 inherently comprises both, and that the dominant process can change over relatively short
34 periods.

35 **Plain Language Summary**

36 We observe calving at a large glacier in Greenland for three weeks, during which we find 8,026
37 calving events across a wide range of environmental conditions. We show that our observation
38 method (radar) agrees well with an independent method (aerial photography). We find that the
39 type of calving varies a lot over time, but that there is no one thing that controls this variation;
40 instead, it is due to a mix of factors. This leads to two kinds of calving events: small chunks
41 falling off the visible part of the front of the glacier, and big chunks toppling over that represent
42 the entire thickness of the front (including the area underwater). Previous work has assumed that
43 glaciers can be grouped by which of these types of calving is more important, but we show that
44 this is an over-simplification at Store, as both these mechanisms are observed and both are the
45 more important mechanism at different times.

46 **1 Introduction**

47 Tidewater glaciers in Greenland drain 88% of the Greenland ice sheet (GrIS) (Rignot &
48 Mouginot, 2012). Ice discharge due to calving from these glaciers is currently responsible for
49 40% (0.33 mm a^{-1}) of GrIS annual net mass loss (global sea-level rise) (Mouginot et al., 2019).
50 While increasing surface melt and runoff act to reduce the solid ice discharge due to the thinning
51 it causes, tidewater glaciers are discharging more ice into the ocean (King et al., 2018).
52 Therefore, understanding how calving occurs and its relationship to other processes in the
53 tidewater-glacier system becomes of central importance in forecasting the evolution of the GrIS
54 in the coming decades and century.
55
56 Calving is an important glaciological process in tidewater environments in which glaciers
57 discharge ice into fjords and coastal seas. It occurs when extensional stresses at the terminus
58 produce fractures that intersect the calving front from either the surface or the base of the glacier
59 (Benn et al., 2017b). Calving is governed by the flow of the glacier and its setting as well as

60   environmental processes that can increase stresses at the terminus, such as buoyancy, surface
61   melting or submarine melt undercutting (Benn et al., 2017b; Benn and Åström, 2018). As such,
62   calving is a highly complex process that happens with little detectable warning based on small
63   changes in one or more of the controlling variables (Åström et al., 2013; Benn et al., 2017a).
64
65   Calving at tidewater glaciers, due to this unpredictable nature, is therefore a difficult process to
66   observe directly, meaning that obtaining information about overall rates or controls, which could
67   allow the development of simple calving parameterisations, is challenging. Conventional remote-
68   sensing does not offer sufficient temporal resolution, with satellites typically providing images a
69   few days apart and even more recent techniques such as Unmanned Aerial Vehicles (UAVs)
70   several hours apart (Chudley et al., 2019; Jouvet et al., 2017; van Dongen et al., 2019). Time-
71   lapse cameras, whilst having sufficient temporal resolution, produce 2D imagery that is not
72   easily converted into 3D volumes of calving events (How et al., 2018; Mallalieu et al., 2017;
73   Vallot et al., 2019). Terrestrial laser scanning has been used (Pętlicki and Kinnard, 2016;
74   Podgórski et al., 2018), but repeat surveys with this technique are problematic due to the large
75   quantity of data in each survey, as well as the significant logistical effort required. Continuous
76   and detailed datasets on calving behaviour at tidewater glaciers are thus lacking, yet
77   understanding this process is crucial to better prediction of tidewater-glacier behaviour and
78   consequent sea-level rise.
79
80   Modelling calving to this end has progressed rapidly in recent years (Benn and Åström, 2018;
81   Todd et al., 2018), but the lack of continuous and detailed observational datasets makes it
82   difficult to validate such models. In this study, we therefore use a real-aperture terrestrial radar
83   interferometer (TRI) (Chapuis et al., 2010; Strozzi et al., 2012; van Dongen et al., 2019;
84   Voytenko et al., 2017; Xie et al., 2019), located 1 km from the front of Store Glacier (Store) to
85   produce a directly observed, near-continuous, 3-week record of calving events for a major
86   Greenlandic outlet glacier. The high resolution of this technique, both spatially and temporally,
87   allows us to characterise 8,026 calving events in terms of size and frequency, while exploring the
88   effect of different environmental factors.
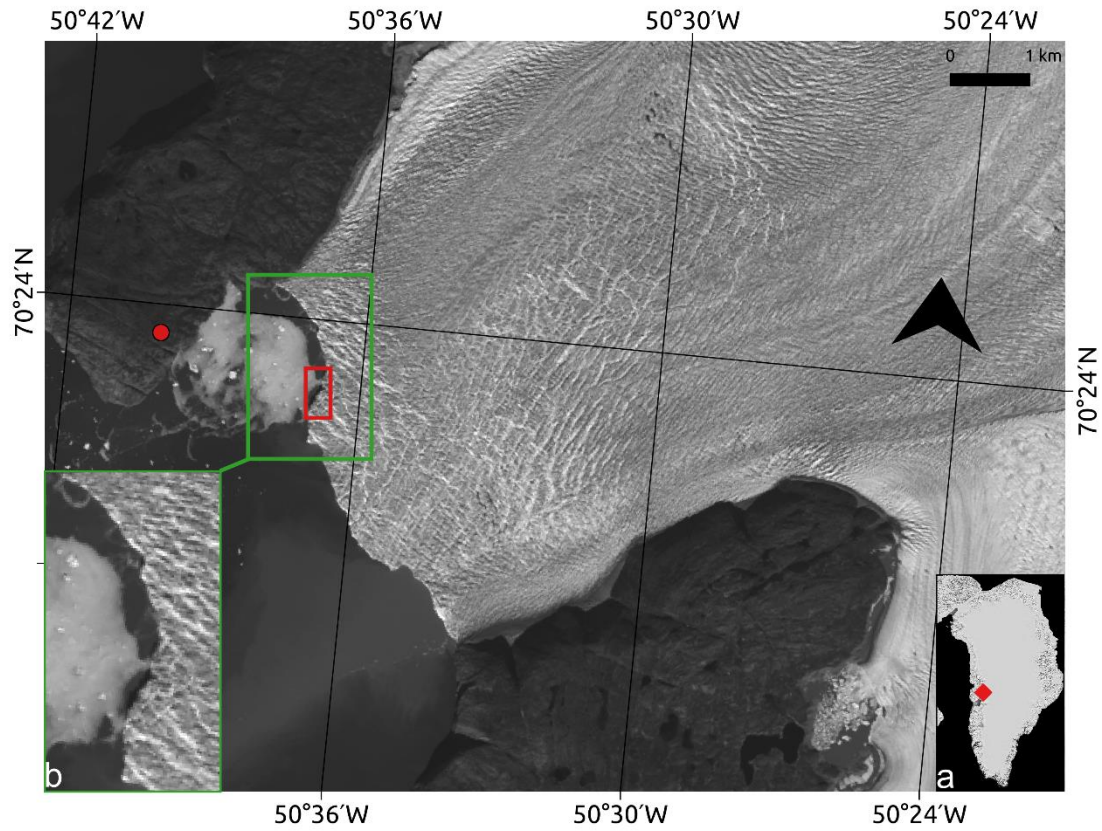
2 Methods

2.1. Study site

Figure 1 – Location of Store Glacier (inset **a**) and location of TRI (red circle). The study area is outlined in green (inset **b**). The red rectangle represents the area zoomed in on in Figures 2 and 3. Background image from Landsat.

95   Store Glacier (*Sermeq Kujalleq*) (70.4° N 50.6° W, Figure 1), referred to here as Store, is one of
96   the largest tidewater outlet glaciers on the west coast of Greenland. The glacier discharges
97   around 12 Gt annually into Ikerasak Fjord (Rignot et al., 2016) in the southern end of
98   Uummannaq Bay. The calving front of Store is 5 km wide, with surface velocities reaching up to
99   6600 m a^{-1} (Joughin, 2018), and is located at a lateral constriction in the fjord on top of a basal
100   pinning point, making the terminus position relatively stable (Todd et al., 2019) with no
101   observed retreat since 1985 (Catania et al., 2018). This stability makes it an ideal target for
102   developing calving models (e.g. Morlighem et al., 2016; Todd et al., 2018; Todd and
103   Christoffersen, 2014; Xu et al., 2013) and for observing tidewater-glacier processes in a
104   'natural', i.e. unperturbed setting. However, behind this pinning point, Store sits in a deep trough
105   that could condition it for rapid retreat should the front be pushed back from the pinning point
106   (Aschwanden et al., 2019). This means Store is additionally interesting, as it may provide
107   information on the transition from a stable calving front to a retreating calving front in the future.

108   2.2. Radar set-up

109   The TRI used in this study was a Gamma Remote Sensing Ground-based Portable Radar
110   Interferometer II (GPRI-II). This is a Ku-band (λ=1.75 cm), real-aperture, rotating instrument
111   that has a range of up to 16 km with a range resolution of 0.75 m and an azimuthal resolution
112   proportional to slant range with a ratio of 8:1000 (i.e., an azimuthal resolution of 8 m at 1 km
113   distance) (Werner et al., 2008). The instrument has one transmit and two receive antenna, spaced
114   25 cm apart, allowing measurement of spatio-temporal change in calving-front dynamics.
115   Velocity can be computed by comparing images from the same antenna taken at two different
116   times; topography, used here, by comparing images from both antennae taken at the same time.
117
118   The GPRI-II was located about 1 km from the glacier terminus on the northern side of the fjord,
119   on a rocky promontory overlooking the calving front (Figure 2). A Canon EOS 750D time-lapse
120   camera was also installed next to it. The instrument was set to scan at a repeat interval of 3
121   minutes for 21 days, between 18:25 on the 5th and 11:01 on the 26th July 2017.
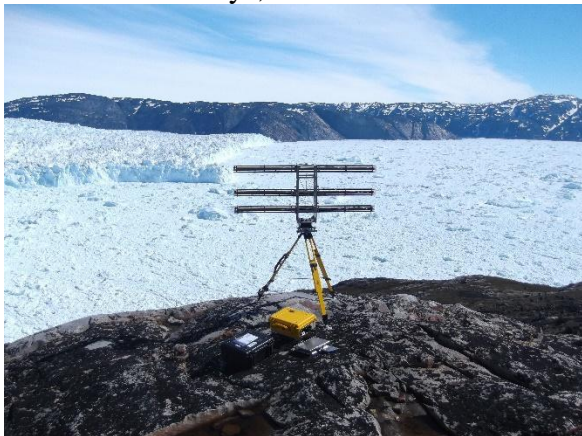

122
123   **Figure 2** – Set-up of the TRI overlooking the calving front of Store.

124   2.3. Radar data processing

125   We used the interferogram record from the TRI, processed using the Gamma software suite, to
126   generate a sequence of digital elevation models (DEMs) from which a record of calving events at
127   Store could be extracted. Topography, which can be computed from the difference in path

128 lengths between the transmitting and receiving antennas, which is related to the measured
129 interferometric phase and wavelength of the radar, was calculated following the method of
130 Strozzi et al. (2012), with the resulting DEMs being resampled to a 10m by 10m resolution and
131 reprojected to Cartesian co-ordinates. As the measurements from each antenna are simultaneous,
132 no atmospheric or phase displacement corrections are needed (Strozzi et al., 2012). Inspection of
133 the resulting record revealed a small number of significant phase breaks and changes in
134 orientation of the TRI over the course of the observation period, which we ascribe to periods of
135 high winds buffeting the instrument. We identified four stable periods, covering the majority of
136 the three-week record (18 out of 21 days), within which orientation and instrument biases were
137 constant. Rotations were applied to each period to ensure alignment of DEMs, as set out in Table
138 1.
139 **Table 1** – Stable periods and applied rotations to ensure alignment. Times are in local Greenland
140 time WGST).

Name	Start	End	Rotation
Period 1	18:25 05/07/17	07:18 14/07/17	0
Period 2	19:06 14/07/17	23:36 18/07/17	-10°
Period 3	14:06 21/07/17	01:03 26/07/17	-3°
Period 4	01:09 26/07	11:01 27/07/17	0

141
142 To identify calving events, we difference consecutive DEMs produced at each timestep within
143 the above periods (Table 1). Initially, we interpolated the DEMs to fill gaps, but this created
144 substantial interpolation artefacts in areas of radar shadow and poor radar return. We therefore
145 avoid interpolation and restrict our analysis to the northern embayment of the calving front (inset
146 **b.** in Figure 1), as the southern embayment was frequently obstructed through the study period
147 by the protruding terminus of Store Glacier, and did not generate good-quality radar returns. This
148 decision means some calving events may be split into several smaller events by no-data pixels,
149 but means that we avoid false positive events. Where DEMs showed anomalous differences (tens
150 of metres of change or more in static surfaces) in elevation values, they were deleted from the
151 record before differencing was undertaken, to leave a consistent set of DEMs within each of the
152 periods identified in Table 1.
153
154 Although no ground control was reliably available within the viewing angle, we have confidence
155 in the data as the remaining DEMs, when considered consecutively, do not show decorrelation
156 within each period. Relative height changes can thus be reliably measured, which is sufficient for
157 our purpose, so we did not pursue a solution to this issue.
158
159 To identify calving events, the remaining DEMs were then differenced within each period,
160 though no differencing was undertaken across different periods. Calving events were then
161 extracted. First, a mask of the ice front position for each period was produced, leaving the area
162 around the calving front, where calving events would be detected, unmasked. The position of the
163 calving front within the unmasked area for each DEM was then digitised using a Sobel filter.
164 Valid calving events were identified as negative changes in elevation of more than 10 m with at
165 least one pixel on the digitised calving front and entirely within the unmasked area. Additionally,
166 events of 3 pixels or fewer in area were filtered out. These steps filtered out noise and avoided
167 detection of negative elevation changes produced by serac collapse inland or iceberg movement

168   or disintegration in the proglacial fjord. The area of each event was then calculated by summing
169   up the number of contiguous DEM pixels meeting the above criteria.

170

171   Finally, the volume of each event was calculated by multiplying the area of each pixel by the
172   elevation change, producing a record of subaerial calving volumes and frequencies for the
173   northern half of Store's terminus. This method therefore imposes a minimum detectable calving
174   event size of 4000 m^3, so smaller events are not part of the analysis in this paper. To support the
175   time-series data, we compare it to total daily surface melt from the Store drainage basin from
176   RACMO 2.3p2 data (van Wessem et al., 2018). We also manually examine the TRI footage to
177   determine when the majority of the northern side of the calving front and fjord were mélange-
178   covered and when at least one plume was visible in the area. Counts and volumes of ice-covered
179   and ice-free periods, and of plume-visible and plume-absent periods, were subsequently
180   standardised to enable direct comparison.

181   3 UAV and time-lapse Data

182   For comparison and validation, we combine TRI data from Store with DEMs produced
183   photogrammetrically with a 20 cm resolution from contemporaneous UAV surveys. Overlapping
184   imagery was captured using a Sony α6000 camera mounted on a Skywalker X8 2m fixed-wing
185   UAV. Flights were flown at an altitude of ≈450 m a.g.l., targeting a ground sampling distance of
186   ≈11 cm, a forward overlap of 80%, and a sidelap of 60%. 3D models were produced using
187   Structure-from-Motion with Multi-View Stereo (SfM-MVS) photogrammetry using Agisoft
188   Metashape software. Models were geolocated via aerial triangulation using a   L1 carrier-
189   phase GPS receiver mounted on the UAV, post-processed kinematically against a bedrock-
190   mounted GPS base station. For a full outline of the methods, see Chudley et al. (2019). We use
191   DEMs produced from flights over the calving front at 2017-07-12 at 22:00 and 2017-07-13 at
192   10:00 WGST. Calving volumes were calculated by differencing the two DEMs, manually
193   delineating the calved area and then multiplying the area of each pixel by the elevation change.
194   Volumes are uncorrected for advance in the position of the glacier front, as the high temporal
195   sampling rate makes this quantity negligible compared to ice loss.

196

197   In addition, we used time-lapse camera images taken at 5-minute intervals throughout the field
198   season, including the 12 hour period separating the two UAV surveys.

199

4 Results

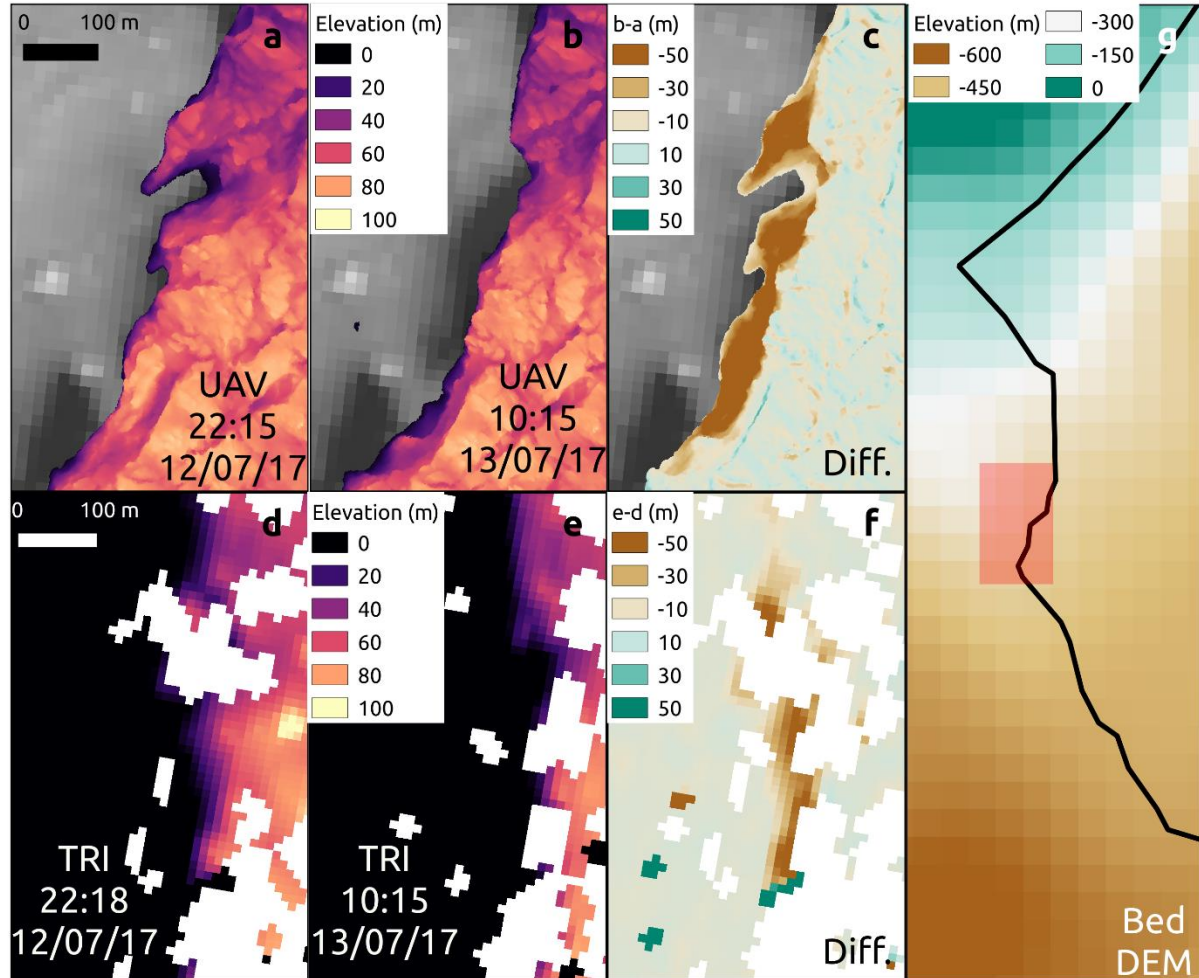4.1. Comparison of TRI with UAV and time-lapse data

Figure 3 – Comparison of calving loss detection across UAV, time-lapse and TRI datasets. Panels **a** and **b** show a large-scale calving loss from UAV-derived DEMs acquired across a 12-hour period; panel **c** shows the difference between panels **a** and **b** Panels **d** and **e** show the same calving loss on TRI-derived DEMs; panel **f** shows the difference between panels **d** and **e** Panel **g** shows the location of the calving at the front of Store (red box) and the bed DEM (see Cook et al. (2020) for its derivation) used in volume calculations. The black line is the approximate outline of the calving front of Store.
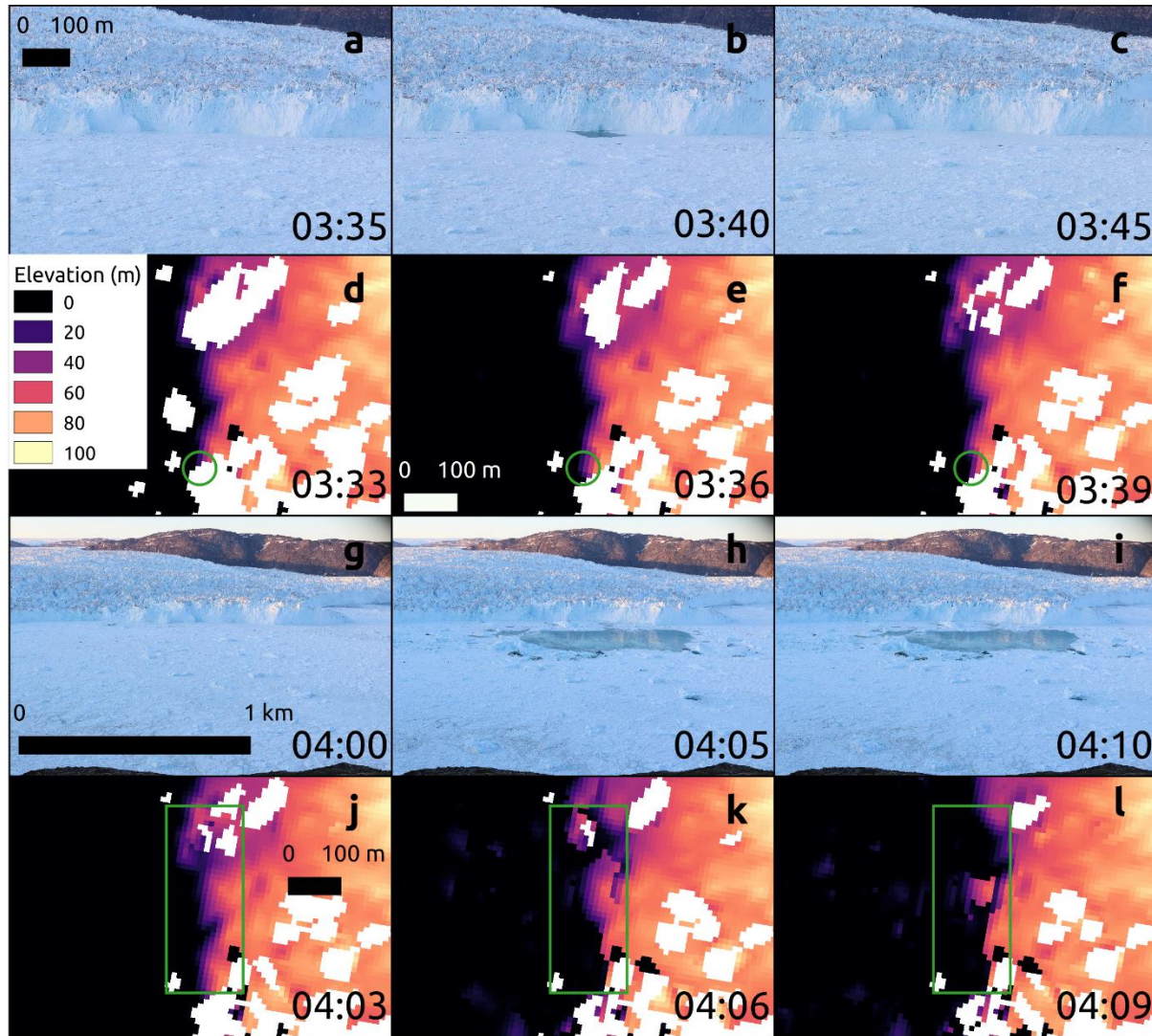
Figure 4 – Comparison of specific calving-event detection across UAV, time-lapse and TRI datasets. Panels **a-c** show a smaller constituent calving event of the total loss in Figure 2 from time-lapse imagery; Panels **d-f** show the same event from the TRI's perspective (event denoted by green circle). Panels **g-i** show the largest constituent calving event of the loss in Figure 2 from time-lapse footage; Panels **j-l** show this event from the TRI's viepoint (inside green box).

Before extracting the full TRI record of calving events, we compare the TRI observations against two contemporaneous high-precision DEMs from UAV surveys separated by 12 hours and time-lapse camera images captured sequentially during this period (Figure 3). The UAV-derived DEMs (Figure 3a-c) show a distinct change in the terminus position, but cannot specify whether calving occurred as a single large event or multiple smaller events for the total ≈1,250,000 m³in subaerial volume loss calculated by differencing the DEMs. This is resolved by the TRI, which captured identical frontal positions (Figure 3d-f) and how terminus geometry changed (Figure 4). With data acquired every 3 minutes, the TRI record reveals a total of 48 individual calving events over the 12-hour period. Figures 4a-c and 4d-f show one of the smaller constituent events, from the perspective of the camera and TRI, respectively, and Figures 4g-i and 4j-l show the largest constituent event, which generated about 40% of the total subaerial volume loss detected

227 over the 12-hour period. As can be seen, the time-lapse and TRI footage both agree on the timing
228 of the calving events. Only 6/48 (12.5%) of the events exceeded a size of $5x10^4$ m^3 (Figure 5),
229 but these larger events were responsible for 56% of the volume loss across the 12-hour period.
230 The smaller events, whilst seven times more numerous, contributed less than half (44%) of the
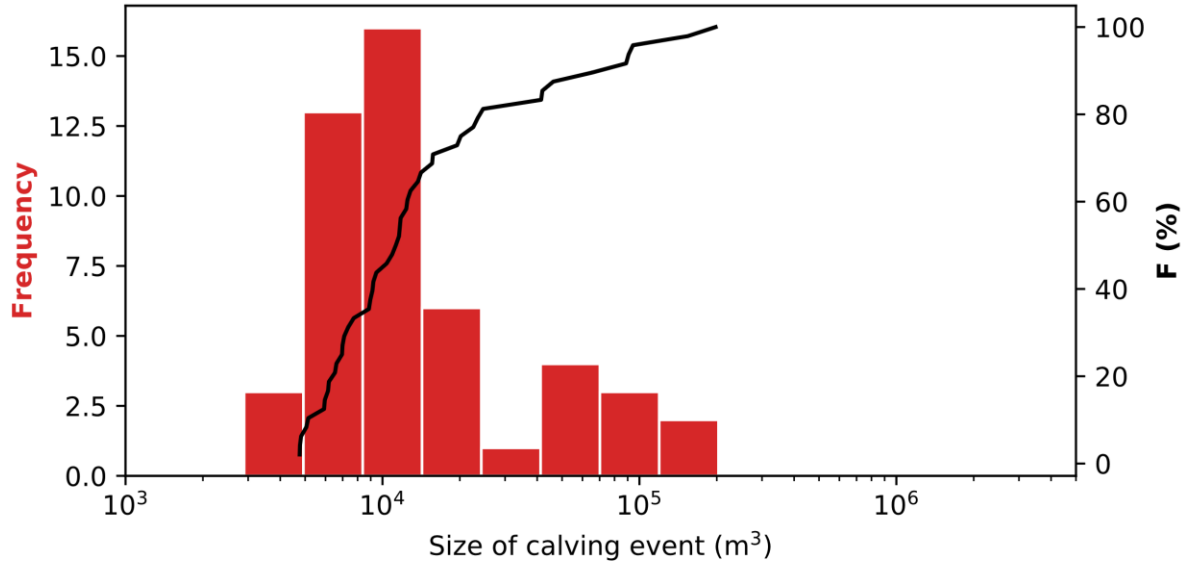231 volume of ice calved.

232
233 **Figure 5** – Cumulative distribution function and histogram of frequency-magnitude relationship
234 of single set of calving events at Store from 22:17 12/07/17 to 10:15 13/07/17. Compare with
235 Figure 6 below.

236 The total subaerial ice volume loss detected by differencing the two UAV DEMs is 1,266,000
237 m^3. When we sum up all the events within the same area detected by the TRI we obtain a total
238 subaerial ice volume loss of 1,240,000 m^3, which is a discrepancy of only 2% compared to the
239 independent UAV method. Assuming that the calving front remains close to vertical, and using
240 the bed DEM shown in Figure 3g, we estimate that the accompanying submarine volume loss is
241 11,900,000 m^3, giving a total calving volume of 13,150,000 m^3. Given that the submarine loss is
242 ≈9 times the subaerial loss derived from the UAV and TRI DEMs, the setting of the glacier is
243 close to floatation.

244 4.2. Calving magnitude-frequency distribution

245 Over the entire three-week period of observations, we find a total of 8,026 calving events with a
246 mean size of 48,428 m^3 (Figure 6). Two thirds of the events by frequency are under 50,000 m^3 in
247 subaerial volume, but these only account for 15% of the total volume loss. Very large events,
248 over 500,000 m^3 in subaerial volume, are very rare, totalling only 35 in the record, or 0.4% of
249 total events, but are responsible for a disproportionate 8% of total volume loss. The middling
250 third (50,000-500,000 m^3) of events by size are consequently responsible for the vast majority of
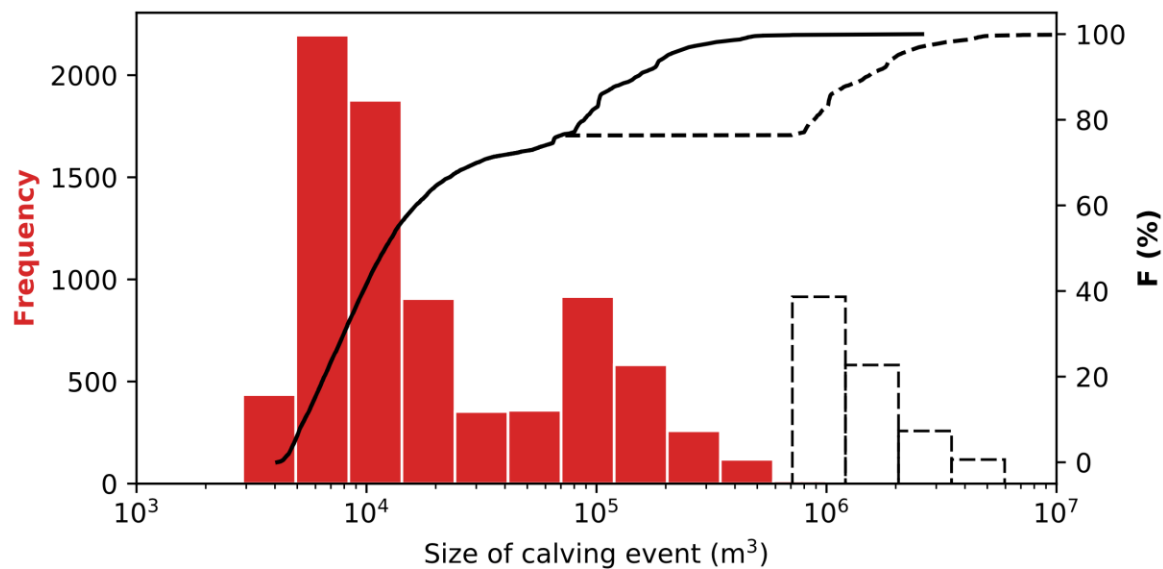251 total volume loss, at 77%.
252

Figure 6 – Cumulative distribution function (right axis) and histogram (left axis) showing size-frequency relationship of all detected calving events observed at Store from 5th July to 27th July 2017. Dashed black bars show posited actual size of full-thickness calving events represented by the second peak in the distribution. Dashed black line shows the cumulative distribution function based on the dashed bars rather than the equivalent red bars. Compare with Figure 5 above. Size refers to the observed subaerial volume.

4.3. Time-varying behaviour in calving

Considering the distribution of calving events over time (Figure 7), we observe low calving activity of <200 events per day prior to 8 July when the fjord was still frozen and filled with mélange. On the 8th, when the mélange broke up, calving activity immediately increased to 300 events, mostly driven by an increase in larger ($>10^5$ m^3) icebergs. From the 9th to the 14th, calving activity increases further, to ≈400 events per day, with a continued high proportion of larger events. From the 15th to the 17th, calving activity declines back to ≈300 events per day, with an especial reduction in the number of the largest ($>10^6$ m^3) category of events, before starting to increase again, on the 18th, with a doubling in the number of the smallest (10^3-10^4 m^3) events. Due to weather interference (high winds buffeting the TRI), there is a data gap on the 19th and 20th. However, the 10 hours of data collected on the 21st show a day of significant calving activity (Figure 7). Calving volumes peak with a value of nearly 2,000,000 m^3 on the 22nd while the daily number of events peaks on the 24th at 721, or 30 events per hour. In general, the number and volume of calving events remain high between the 18th and 24th, though volumes are lower from the 23rd onwards.
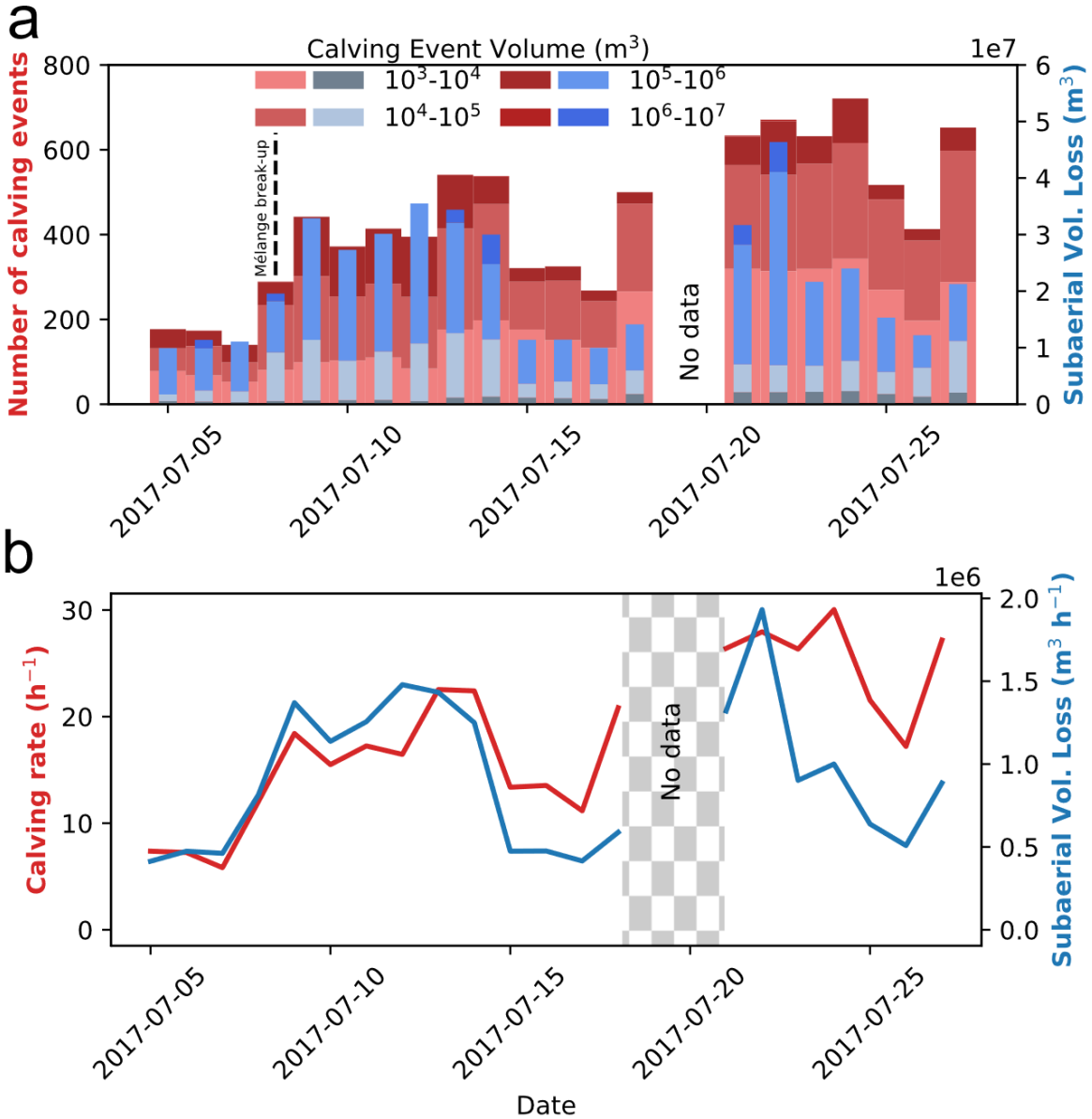
Figure 7 – Time series of calving events at Store. **a** Bars stacked by volume of event. Daily counts are shown by red bars; cumulative volumes by the blue bars. **b** Hourly calving rate. Note greater calving activity from the 8th to the 14th.

A possible trigger for calving activity is the weather or, more specifically, surface melt variations due to changes in air temperature, as greater surface melt is hypothesised to enhance the depth of surface crevasse penetration (Benn & Åström, 2018). We examine this by plotting calving counts and volumes (Figure 8) against surface melt for the Store basin, derived by integrating surface runoff from the RACMO dataset across the Store basin. Ignoring days with incomplete or no calving data, we find correlation coefficients of 0.42 for the counts, which is significant at the 95% confidence interval, but only 0.12 for the volumes, which is statistically insignificant.
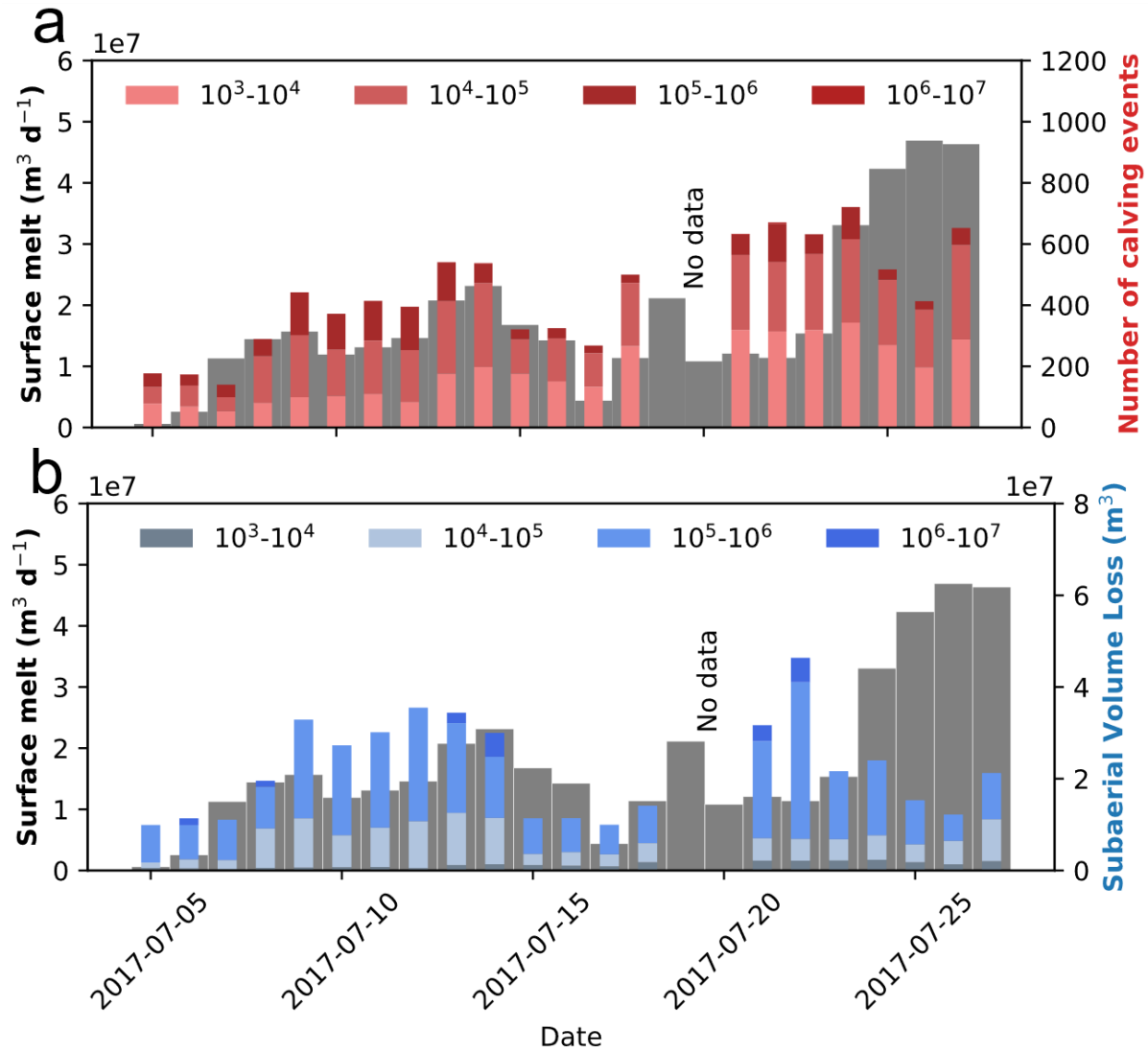
287

Figure 8 – Time series of calving events and surface melt derived from RACMO 2.3p2 data. **a**
shows calving counts (red bars) and **b** calving volumes (blue bars).

To examine any diurnal variation in calving activity, we pick four days (Figure 9), each
representative of one period of calving activity: the 6th, for the pre-mélange-break-up state of
calving; the 11th, in the period of sustained higher calving following break-up; the 15th, in the
following period of lower calving; and the 23rd, for the second period of higher calving.
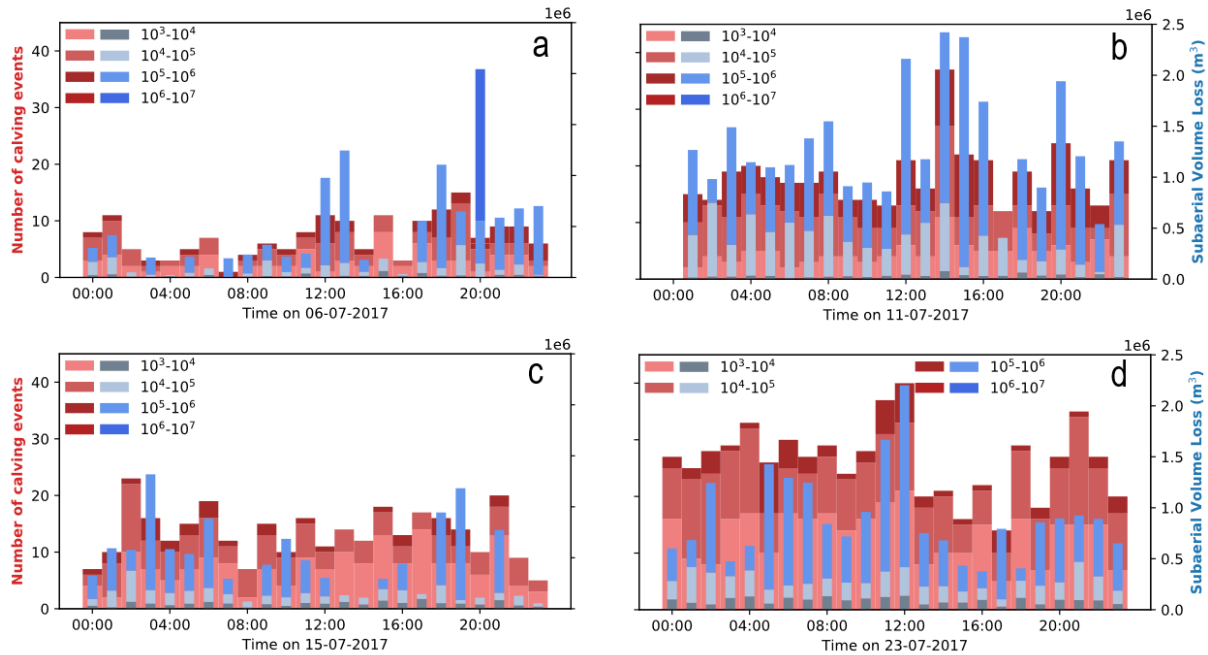
Figure 9 – Time series of calving binned by hour from **a** 06/07/2017 (before mélange breaks up), **b** 11/07/2017 (high calving activity following mélange break-up), **c** 15/07/2017 (reduced calving activity), and **d** 23/07/2017 (renewed high calving activity).

As Figure 9 shows, there is very little discernible consistent pattern in calving activity; the only consistent feature across all four days shown is a peak in counts and volumes at 12:00±2 hours WGST. On the 6th July (Figure 9a), whilst the mélange was still intact, the midday peaks occur at 12:00 (counts) and 13:00 (volumes), with very little calving for the whole morning (only 01:00 exceeds a rate of 10 events per hour). Calving then drops off into the afternoon before reviving from 17:00 through the evening. On the 11th July (Figure 9b), after mélange break-up, we see high calving all day, with both midday peaks at 12:00, followed by another peak at 14:00. The later afternoon and evening are more variable than the morning, but calving rates only fall well below 15 per hour at 17:00 and 22:00. In the lull in calving activity following the post-break-up peak, represented by the 15th July (Figure 9c), calving counts show little discernible pattern, though are perhaps consistently higher in the morning than the evening; rates per hour, however, stay below 20 for nearly the whole day. Calving volumes show a clearer morning peak, midday peak (at 10:00) and then an evening peak, with reduced activity in-between these. In the final period of calving we observe, the second period of high activity, as shown for the 23rd July (Figure 9d), we see once more a clear midday peak at 12:00, with an afternoon depression in both calving counts and volumes. Evening and morning activity, though, are broadly comparable. We also investigated whether a link between the tidal cycle and calving activity could be discerned, but found no statistically significant relationship in this dataset.

4.4. Spatial variations in calving

Two major factors that are hypothesised to influence calving rates are the presence/absence of mélange in the fjord and of active meltwater plumes fed by subglacial discharge. We assess the impact of both of these at Store by comparing calving counts and volumes for periods of mélange presence and absence and of visible plume presence and absence (Figure 10). In both

321 cases, the counts and volumes are expressed as an average rate per day. We observe more than a
322 doubling in the number of calving events in the absence of mélange (from 271 events per day
323 with mélange to 588 events without), compared to when it is present, and a concomitant 44%
324 increase in volumes. In the presence of visible plumes, the number of calving events increases by
325 70%, from 395 per day to 672, but the volume loss from these events only increases very
326 slightly, by 3%, compared to when no plumes are visible.
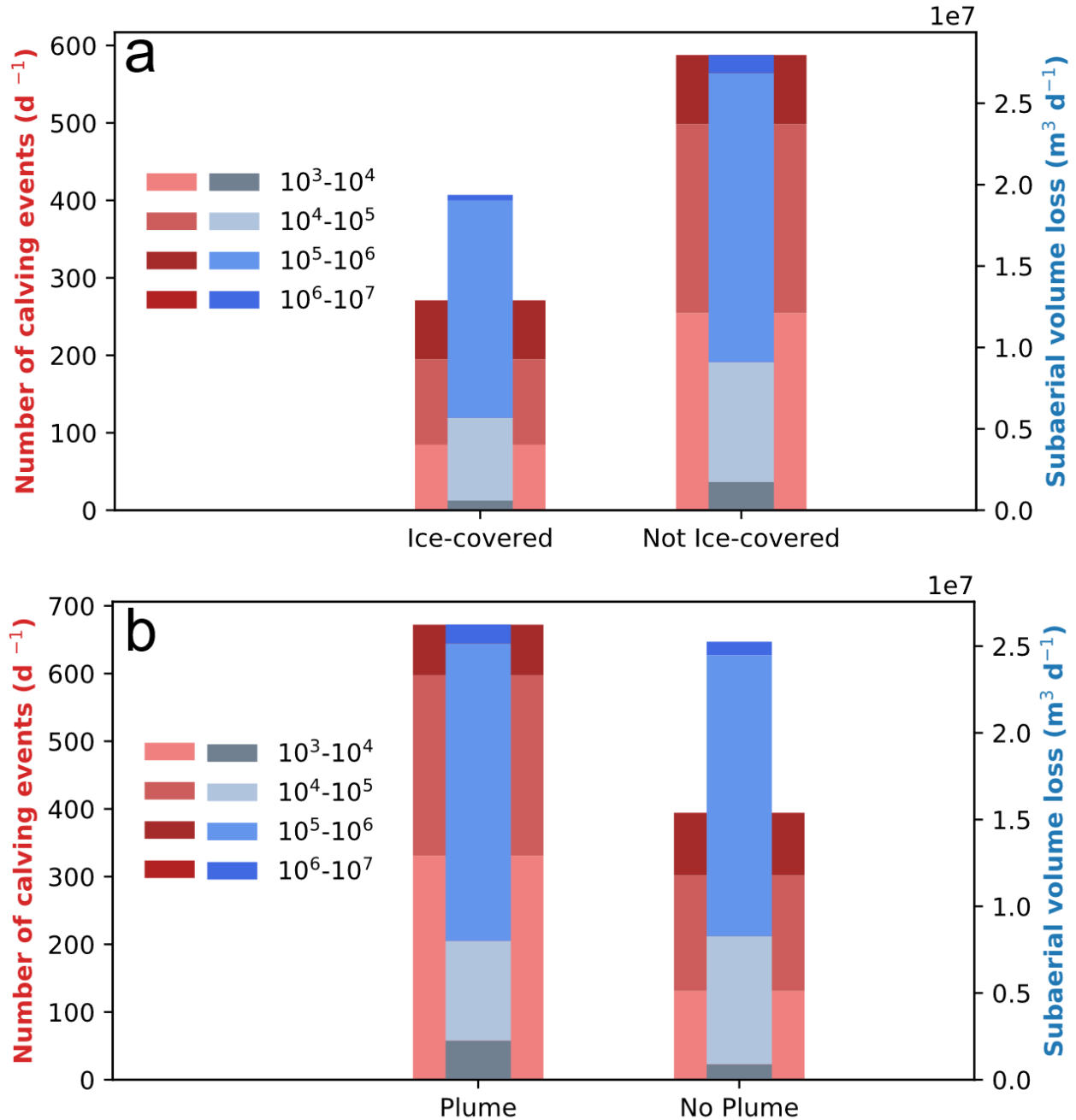

327
328 **Figure 10** – Calving event counts and volumes on average per day for **a** when mélange is present
329 compared to when it is not. Note how mélange presence suppresses calving; and **b** when plumes
330 are visible compared to when they are not. Note how plume presence leads to more, smaller and
331 mid-size calving events.

332   **5 Discussion**

333   5.1. Calving behaviour

334   The observed magnitude-frequency distribution of calving shows an inverse relationship (Figure
335   6): there are far more smaller events than larger ones, though the rarer larger events account for
336   most of the volume loss. The smaller events mostly represent occurrences similar in style to that
337   shown in Figure 4a-f, i.e. detachment of relatively small blocks of ice from the subaerial portion
338   of the calving front that then fall into the fjord. The larger events are instead exemplified by
339   Figure 4g-l, where entire sections of the front peel off and topple over. No large tabular-style
340   calving events are observed here; at Store, these events usually happen on the floating southern
341   part of the calving front and not on the grounded northern section analysed here (Todd et al.,
342   2018). Contrary to other observations (Åström et al., 2014; Chapuis and Tetzlaff, 2014), the
343   calving events discussed here do not follow a clear power-law distribution (Figure 6), with the
344   cumulative distribution across the entire dataset suggesting a bimodal sequence of calving events
345   (Figure 11). One peak is at a magnitude of the order of 10^4 m^3, with another on the order of 10^5
346   m^3. We hypothesise that the first peak represents the smaller calving events described above,
347   where only a (relatively) small subaerial portion of the calving front calves. The second peak
348   then represents the larger calving events in which a larger portion of the front breaks off. We
349   explain the bimodal event size distribution (with a paucity of intermediate sized events) to be due
350   to the mechanics of fracture propagation: if a fracture reaches the waterline, it will usually fill
351   with water, which will propagate it deeper, which will further increase the water pressure in a
352   positive feedback. It is also possible that surface fractures will intersect basal crevasses that
353   propagate upwards from the base (Todd et al., 2018). Both of these mechanisms can generate
354   large, full-thickness calving events. The first peak consequently represents those events where
355   the initiating fracture does not reach the waterline, limiting calving to detachment of blocks on
356   the subaerial region of the calving front; the second peak represents those where the fracture has
357   reached the waterline and continued to the base, or intersected a basal crevasse, resulting in
358   events that are an order of magnitude greater or even larger. Because our observations are limited
359   to the subaerial portion of the front and we know the terminus is close to floatation, the larger
360   events reported with a modal peak of 10^5 m^3 may be the subaerial portion of events with a true
361   modal size closer to 10^6 m^3 (as shown by dashed black lines in Figure 6). As such, intermediate
362   events are rare, because detachment of bloacks can only be so large (i.e. a few tens of metres of
363   ice thickness across a small section of the front) whereas the large toppling of bergs can only be
364   so small (i.e. hundreds of metres of ice thickness across a larger portion of front).
365
366   Returning to how previous calving datasets have shown a power-law distribution for the
367   magnitude-frequency of events, we hypothesise that this is due to the relatively short duration of
368   previous observations. The bimodality we observe here is a result of two characteristic iceberg
369   size distributions: one being small blocks of ice falling off the front due to instability from
370   fractures that are tens of metres deep and the other being larger bergs forming when fractures
371   penetrate the whole ice-column. Superimposed on this bimodality is a time-varying calving
372   behaviour (Figure 11). In the days leading up to mélange break up on the 8th, this bimodality is
373   evident in a similar pattern to that found for the whole dataset. Thereafter, from the 8th through to
374   the 13th, there is a higher-than-average representation of the larger class of calving events while
375   the smaller class is under-represented, before the 14th returns to near the overall distribution.
376   After the 14th, however, the rest of the dataset tends towards a relative under-representation of

377 the larger events, while the smaller events are more frequent than average. Therefore, if our
378 observations had been limited to a few days only, e.g. as shown in Figure 5, we might have
379 concluded that a power law fitted on the slope of the cumulative distribution function would be
380 an accurate representation of the data; yet this slope varies greatly over the period of
381 observations (Figure 11). We therefore suggest that, to get an accurate picture of the calving
382 distribution at a tidewater glacier, detailed observations of calving need to be maintained for at
383 least a week, ideally for a fortnight or even longer. Shorter observational periods run the risk of
384 missing out on aspects or distinct periods of calving behaviour or of attempting to fit a single
385 power law to a distribution that might have multiple distinct causes, each best-represented by a
386 single power law. In the case presented here, a separate power law, based on the variety of
387 cumulative distribution functions we observe (Figure 11), would be needed for a) the system
388 before mélange break-up (5th-7th), b) the system in the immediate aftermath of mélange break-up
389 (8th-14th), and c) the system in the later post-break-up period (15th-27th) (Figure 8, Figure 11).
390 Doing so, we find best-fit power laws with exponents of 0.53, 0.64 and 0.57, respectively, and R^2
391 values of 0.58, 0.73, and 0.44, respectively, suggesting that this calving dataset is mostly poorly
392 represented by power laws, with the possible exception of the immediate post-mélange-break-up
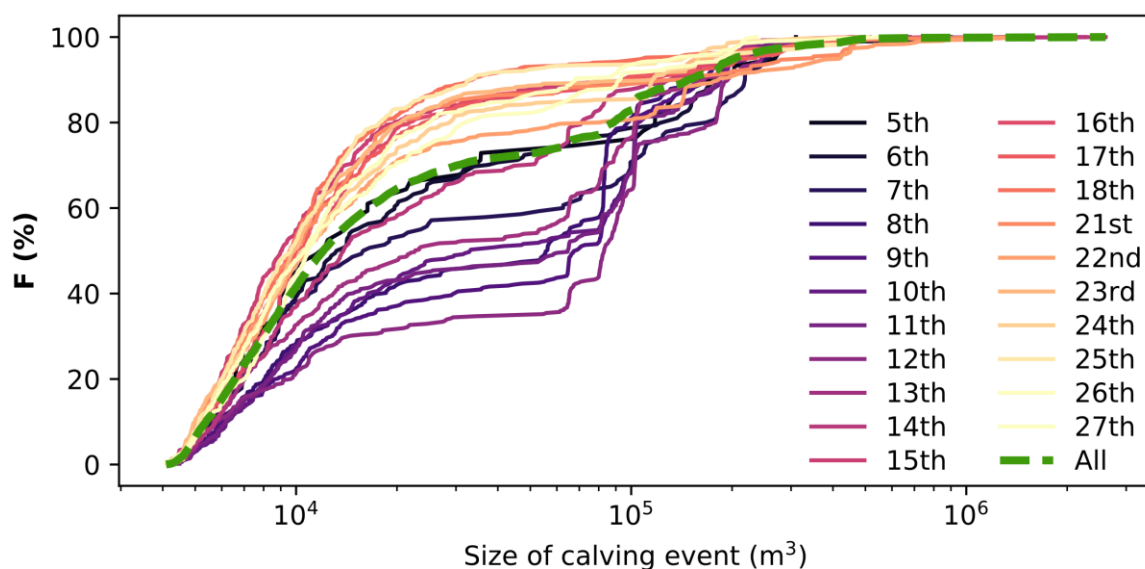393 period, though, even in this period, we still observe pronounced bimodality.

394
395 **Figure 11** – Cumulative distribution function for calving events observed from 5th July to 27th
396 July 2017, with coloured lines denoting distribution on specific days and dashed green line
397 showing the overall distribution. Notice how days earlier in the observation period cluster below
398 the overall average distribution, whereas those later in the period cluster above it.

399 5.2. Calving controls

400 The TRI record from Store provides some interesting information on the global distribution and
401 controls on calving. We find a sustained 6-day period of higher calving activity in the aftermath
402 of mélange break-up on the 8th July (Figure 7), with rates more than doubling compared to before
403 break-up. Previous modelling work on Store (Todd et al., 2018) suggests this corresponds to the
404 loss of backstress from the mélange, which provides a resisting force when the mélange is rigid.
405 When the backstress is lost, this force disappears, facilitating crevasse propagation of sufficient

406 depth to trigger detachment of full-thickness sections of the front (Amundson & Truffer, 2010).
407 As such, we find the highest proportions of the largest events at this time, with the largest two
408 categories of events ($>10^5$ m^3 in terms of subaerial volume and potentially $>10^6$ m^3 in total
409 volume) making up an average of 33% of all events between the 9th and the 12th, inclusive,
410 compared to an average of 24% beforehand and 11% afterwards. We then see a period of
411 renewed calving intensity from at least the 21st to the 24th, this time predicated on smaller events,
412 which seems to tail off on the 25th and 26th before possibly starting to pick up again on the 27th,
413 the very last day of the record. An interesting perspective on this behaviour is provided by the
414 theory of calving fronts as self-organised critical systems (Åström et al., 2014; Chapuis &
415 Tetzlaff, 2014), whereby the front continually oscillates around a critical point that is determined
416 by the environmental boundary conditions – air and water temperature, bed topography, glacier
417 geometry, etc. Fronts that are subcritical will tend to move towards the critical point, building up
418 instabilities and manifesting small-scale, subdued calving behaviour. At some point, the calving
419 front will find itself in a state of supercriticality due to a change in the environment or as it
420 overshoots the critical point, which produces large-scale, sustained calving as the system adjusts
421 back towards the critical point. Here, therefore, removal of the mélange can be interpreted as
422 shifting the critical point of the system, suddenly placing the calving front of Store in a position
423 of overshoot, and therefore supercriticality, manifested through a series of large calving events
424 (the initial period of strong calving from the 8th-13th). The now-subcritical system then steadily
425 re-advances towards the critical point, building up instabilities as it does so, and exhibiting small
426 calving events (the quieter period of calving from the 14th to the 18th). Although greater calving
427 activity is observed subsequent to this until the end of the record (the 19th to the 27th), the shape
428 of the cumulative distribution functions (Figure 11), with a marked dominance of smaller events,
429 suggests this is a prolongation of the subcritical phase, rather than a return to supercriticality.
430
431 This theory also helps to explain the very poor correlation found between calving event size and
432 amount of surface melt (Figure 8). Whilst there is statistically significant correlation between
433 surface melt and the *number* of calving events (Figure 8a), there is none between surface melt
434 and the *volume* of events (Figure 8b). Increased surface melt should enhance fracture
435 propagation by increasing the amount of water available for hydrofracturing at the surface, or by
436 generating more vigorous freshwater-plume circulation at the front, leading to increased
437 submarine melting and undercutting (O'Leary & Christoffersen, 2013) – this link is discussed
438 further, below. Hence we would expect to find a link between surface melt and counts of calving
439 events. Whether these fractures grow in such a way as to produce large or small calving events,
440 however, would seem to be primarily determined by other factors, such as whether the system is
441 in a subcritical or supercritical state.
442
443 A link between surface melt and calving activity is also observed (Figure 8), as shown by the
444 consistent appearance of a midday peak, the most plausible explanation for which is that this
445 time of day has the greatest amount of insolation and therefore surface melt, thus driving fracture
446 propagation. However, this midday peak is the daily peak on only two out of the four days
447 examined in Figure 9: the 11th and 23rd July (Figure 9b and 9d); on the other two days, the daily
448 peak occurs at 19:00-20:00 (6th July; Figure 9a) and 02:00-03:00 (15th July; Figure 9c),
449 reinforcing the conclusion that surface melt is just one driver of calving and not necessarily the
450 most important.
451

452   We also examine two important factors contributing to the criticality of the system (Figure 10).
453   In accordance with the pattern of activity observed in Figure 7, we find much stronger calving
454   activity in the absence of mélange compared to when it is present (Figure 10a; compare Figure
455   7). One point worth noticing is that the largest of two observed modal peaks in calving accounts
456   for a greater proportion (28%, representing 888 events) of the total calving count when mélange
457   is present compared to when it is not (15%, representing 1041 events), suggesting that mélange
458   presence preferentially suppresses smaller events, but is relatively ineffective at holding back
459   larger events, which will calve regardless once they become sufficiently unstable.

461   However, a calving front exhibiting self-organised critical behaviour near its critical point should
462   show calving activity that follows a power-law distribution with exponents in the range 1.06-
463   1.46 (Åström et al., 2014), which we do not observe in this study. On the other hand, we do
464   observe qualitative changes in calving behaviour between a likely subcritical calving phase (5th-
465   7th; dominated by smaller events), a likely supercritical phase (8th-14th; dominated by larger
466   events) and a second subcritical phase (15th-27th; dominated by smaller events), with the period
467   of subcriticality representing over 2/3 of the record duration. These features are consistent with a
468   calving front operating in a self-organised critical regime (Åström et al., 2014). It is also worth
469   noting that, for grounded tidewater margins, which is the relevant category for the northern part
470   of Store's calving front, the power law is expected to display an exponential cut-off for calving
471   events with volumes over 10^4 m^3 (Åström et al., 2014). If we only consider the events below this
472   volume threshold and repeat the power-law analysis described in Sect. 4.1, we find R^2 values of
473   0.83, 0.77, and 0.78, respectively. These represent a significant improvement in R^2 values for the
474   two putatively subcritical phases and little change for the putatively supercritical phase, which is
475   consistent with grounded calving fronts operating in a self-organised critical regime (Åström et
476   al., 2014). The power-law exponents, however, jump to 3.66, 3.73 and 3.64 when considering
477   events below this 10^4 m^3 threshold, which is much higher than expected. We attribute this to our
478   processing method excluding events below 4000 m^3 in size, distorting the tail of the distribution.
479   Therefore, we suggest that the calving front at Store exhibits behaviour that is at least
480   qualitatively consistent with self-organised criticality and potentially provide quantitative
481   support for this. This point also reinforces our assertion that calving behaviour changes over time
482   and thus cannot be necessarily well-represented or modelled by a short time series of
483   observations.

485   We additionally show that visible active meltwater plumes, driven by surface melt, encourage
486   more frequent calving events (Figure 10b), possibly as a response to undercutting of the calving
487   front, as described above. What is less intuitive is that the increase in the number of events is
488   associated with barely any increase in the volume loss from calving. The presence of plumes in
489   this study greatly increases the number of smaller ($<10^5$ m^3) calving events at the expense of the
490   larger events ($>10^5$ m^3), which fall from 24% (representing 909 events) to 11% (representing 730
491   events) of the total event count. We attribute this to plume-induced melting making it 'easier' for
492   blocks and small vulnerable sections of the front to break off, removing them consecutively in a
493   relatively high number of events before instabilities can build up in the ice and thereby reducing
494   the frequency of large calving events. This does not mean plumes reduce the total mass loss as
495   we are unable to observe the quantity of ice lost by plume-induced melting, or calving, taking
496   place below the waterline. The finding does, nonetheless, highlight that the relationship between

497 plumes and calving is not as straightforward as previously proposed (O'Leary & Christoffersen,
498 2013).
499

500 Also, the bimodal distribution of iceberg sizes found in this study of Store shows that
501 classification of glaciers into types that produce either small magnitude icebergs by serac failure
502 or large icebergs by full-thickness capsizing slabs, with Store falling in the latter category (Fried
503 et al., 2018), may be too simplistic since both types of events are observed to occur frequently at
504 Store. While it is possible that some glaciers will calve mostly by one mechanism and that others
505 will calve mostly by the other, our TRI record from Store indicates that the calving mechanism
506 inherently comprises both and that the predominant calving style can change from one type to
507 the other over relatively short periods. This finding is a result of the extremely high resolution of
508 the TRI, which recorded calving every 3 minutes. While our UAV investigation showed a
509 subaerial volume loss of 1,250,000 m^3 from a frontal retreat between two surveys separated by
510 12 hours (Figure 4), the TRI showed this retreat was comprised of 48 individual events and that
511 iceberg sizes varied by two orders of magnitude or more (Figure 5). This finding indicates that
512 there are inherent limitations in the use of remotely sensed images to discern calving styles and
513 that classification of calving glaciers may regure size-frequency distributions and assessment of
514 probability (Figure 6, Figure 11).

515 5.3. Limitations and validation

516 This study has produced one of the longest records of calving from the use of a TRI. The
517 instrument captured calving events occurring over half of the calving front of Store during three
518 weeks in July 2017. Overall, we found a very good agreement between the volumetric loss of ice
519 in a multitude of calving events with those estimated from the UAV-derived DEMs produced at
520 a 0.2 m resolution (Figure 3, Figure 4). This gives us confidence that the TRI was successful in
521 identifying calving events on the northern side of Store and that the TRI analysis has produced
522 accurate volumetric estimates However, due to the 5-km-wide calving front, it was not possible
523 to also survey calving taking place in the southern half of the terminus, where numerical
524 modelling indicates the largest, tabular-style calving events are most likely to occur (Todd et al.,
525 2018). However, our study shows that the northern terminus is very close to floatation and thus
526 that the differences between southern half and northern half may not be so pronounced.
527 The data processing method for the TRI data also introduces some errors – notably, we are
528 unable to distinguish events smaller than 4000 m^3 in volume and some events near this limit may
529 have been erroneously excluded from the analysis. A more fundamental issue is that, obviously,
530 the TRI only provides information on the subaerial volumes of calving events, which means the
531 identified volumes of the larger events are only partial. As computed in Section 4.1, we find a
532 nine times greater submarine calving volume than the subaerial volume from UAV and TRI
533 DEMs for the sequence of calving events displayed in Figures 2 and 3. This shows that the
534 calving front in this location is at or very close to floatation, and hence that the observed modal
535 peak in the subaerial calving volume of larger events represents only 1/10th of the actual iceberg
536 size. The modal peak of the smaller iceberg size may, however, be close to the actual volume
537 given that these events represent relatively small blocks falling off the front.
538

539 **6 Conclusions**

540 We present a novel 3-week-long record of calving events at Store Glacier from a TRI survey that
541 includes the transition from a mélange-filled proglacial fjord setting to a mélange-free
542 environment. The record includes a total of 8,026 calving events with a mean volume of 4.8 x
543 10^4 m^3. Maximum calving rates peak at 30 events per hour, or 720 per day, with an average rate
544 of 17 events per hour, or 408 per day. This dataset suggests mélange presence preferentially
545 suppresses smaller calving events and that mélange break-up leads to a prolonged period of
546 higher calving activity at Store, with calving rates near-doubling in ice-free conditions. We
547 assess the reliability of this dataset by making a comparison to a set of calving events
548 independently recorded across a 12-hour period in UAV data and find a mismatch of only 2%,
549 giving us confidence in the validity of the results presented here. With the TRI capturing calving
550 events in high resolution, both spatially and temporally, we find a bimodal size-frequency
551 distribution of events that reflects two specific types of calving: blocks and relatively small
552 sections of ice breaking off the subaerial part of the terminus with a characteristic modal size of
553 10^4 m^3, and much larger icebergs released from full-thickness failure. While the observed modal
554 size of the latter is 10^5 m^3, we estimate the actual volume to be closer to 10^6 m^3 since our
555 observations capture only the subaerial portion of the terminus, which is at or near floatation.
556 However, we find the predominant type of calving can change from small to large events over
557 relatively short periods.
558
559 With both temporal and spatial variability in calving at Store, our observations do not support
560 any simple power-law relationship between iceberg size and frequency. Instead, we observe a
561 complex relationship between calving and the presence of visible meltwater plumes at the
562 calving front. Plume presence leads to 70% more calving events, but the subaerial volume of ice
563 detaching from the terminus in these events only increases by 3%. We relate this to reduced
564 support due to plume-induced melting allowing unstable ice blocks to calve earlier than they
565 might otherwise have done. We further find little relationship between surface melt and calving
566 volumes, though a statistically significant one between surface melt and calving counts, again
567 indicating the complexities underlying calving behaviour.

References

Amundson, J. M., & Truffer, M. (2010). A unifying framework for iceberg-calving models. *Journal of Glaciology*, *56*(199), 822–830. https://doi.org/10.3189/002214310794457173

Aschwanden, A., Fahnestock, M. A., Truffer, M., Brinkerhoff, D. J., Hock, R., Khroulev, C., et al. (2019). Contribution of the Greenland Ice Sheet to sea level over the next millennium. *Science Advances*, *5*(6), eaav9396. https://doi.org/10.1126/sciadv.aav9396

Åström, J. A., Riikilä, T. I., Tallinen, T., Zwinger, T., Benn, D., Moore, J. C., & Timonen, J. (2013). A particle based simulation model for glacier dynamics. *The Cryosphere*, *7*(5), 1591–1602. https://doi.org/10.5194/tc-7-1591-2013

Åström, J. A., Vallot, D., Schäfer, M., Welty, E. Z., O'Neel, S., Bartholomaus, T. C., et al. (2014). Termini of calving glaciers as self-organized critical systems. *Nature Geoscience*, *7*(12), ngeo2290. https://doi.org/10.1038/ngeo2290

Benn, D. I., & Åström, J. A. (2018). Calving glaciers and ice shelves. *Advances in Physics: X*, *3*(1), 1513819. https://doi.org/10.1080/23746149.2018.1513819

Benn, D. I., Cowton, T., Todd, J., & Luckman, A. (2017). Glacier Calving in Greenland. *Current Climate Change Reports*, 1–9. https://doi.org/10.1007/s40641-017-0070-1

Benn, D. I., Åström, J., Zwinger, T., Todd, J., Nick, F. M., Cook, S., et al. (2017). Melt-under-cutting and buoyancy-driven calving from tidewater glaciers: new insights from discrete element and continuum model simulations. *Journal of Glaciology*, 1–12. https://doi.org/10.1017/jog.2017.41

Catania, G. A., Stearns, L. A., Sutherland, D. A., Fried, M. J., Bartholomaus, T. C., Morlighem, M., et al. (2018). Geometric Controls on Tidewater Glacier Retreat in Central Western Greenland. *Journal of Geophysical Research: Earth Surface*, *123*(8), 2024–2038. https://doi.org/10.1029/2017JF004499

603   Chapuis, A., & Tetzlaff, T. (2014). The variability of tidewater-glacier calving: Origin of event-

604   size and interval distributions. *Journal of Glaciology*, *60*(222), 622–634.

605   https://doi.org/10.3189/2014JoG13J215

606   Chapuis, A., Rolstad, C., & Norland, R. (2010). Interpretation of amplitude data from a ground-

607   based radar in combination with terrestrial photogrammetry and visual observations for

608   calving monitoring of Kronebreen, Svalbard. *Annals of Glaciology*, *51*(55), 34–40.

609   https://doi.org/10.3189/172756410791392781

610   Chudley, T. R., Christoffersen, P., Doyle, S. H., Abellan, A., & Snooke, N. (2019). High-

611   accuracy UAV photogrammetry of ice sheet dynamics with no ground control. *The*

612   *Cryosphere*, *13*(3), 955–968. https://doi.org/10.5194/tc-13-955-2019

613   van Dongen, E., Jouvet, G., Walter, A., Todd, J., Zwinger, T., Asaji, I., et al. (2019). Tides

614   modulate crevasse opening prior to a major calving event at Bowdoin Glacier, Northwest

615   Greenland. *Journal of Glaciology*, 1–11. https://doi.org/10.1017/jog.2019.89

616   Fried, M. J., Catania, G. A., Stearns, L. A., Sutherland, D. A., Bartholomaus, T. C., Shroyer, E.,

617   & Nash, J. (2018). Reconciling drivers of seasonal terminus advance and retreat at

618   thirteen central west Greenland tidewater glaciers. *Journal of Geophysical Research:*

619   *Earth Surface*, *0*(ja). https://doi.org/10.1029/2018JF004628

620   How, P., Schild, K., Benn, D., Noormets, R., Kirchner, N., Luckman, A., et al. (2018). Calving

621   controlled by melt-under-cutting: detailed calving styles revealed through time-lapse

622   observations. *Annals of Glaciology*. Retrieved from https://doi.org/10.1017/aog.2018.28

623   Jouvet, G., Weidmann, Y., Seguinot, J., Funk, M., Abe, T., Sakakibara, D., et al. (2017).

624   Initiation of a major calving event on the Bowdoin Glacier captured by UAV

625 photogrammetry. *The Cryosphere*, *11*(2), 911–921. https://doi.org/10.5194/tc-11-911-

626 2017

627 Mallalieu, J., Carrivick, J. L., Quincey, D. J., Smith, M. W., & James, W. H. M. (2017). An

628 integrated Structure-from-Motion and time-lapse technique for quantifying ice-margin

629 dynamics. *Journal of Glaciology*, *63*(242), 937–949. https://doi.org/10.1017/jog.2017.48

630 Morlighem, M., Bondzio, J., Seroussi, H., Rignot, E., Larour, E., Humbert, A., & Rebuffi, S.

631 (2016). Modeling of Store Gletscher's calving dynamics, West Greenland, in response to

632 ocean thermal forcing. *Geophysical Research Letters*, *43*(6), 2016GL067695.

633 https://doi.org/10.1002/2016GL067695

634 Mouginot, J., Rignot, E., Bjørk, A. A., van den Broeke, M., Millan, R., Morlighem, M., et al.

635 (2019). Forty-six years of Greenland Ice Sheet mass balance from 1972 to 2018.

636 *Proceedings of the National Academy of Sciences*, 201904242.

637 https://doi.org/10.1073/pnas.1904242116

638 O'Leary, M., & Christoffersen, P. (2013). Calving on tidewater glaciers amplified by submarine

639 frontal melting. *The Cryosphere*, *7*(1), 119–128. https://doi.org/10.5194/tc-7-119-2013

640 Pętlicki, M., & Kinnard, C. (2016). Calving of Fuerza Aérea Glacier (Greenwich Island,

641 Antarctica) observed with terrestrial laser scanning and continuous video monitoring.

642 *Journal of Glaciology*, *62*(235), 835–846. https://doi.org/10.1017/jog.2016.72

643 Podgórski, J., Pętlicki, M., & Kinnard, C. (2018). Revealing recent calving activity of a tidewater

644 glacier with terrestrial LiDAR reflection intensity. *Cold Regions Science and Technology*,

645 *151*, 288–301. https://doi.org/10.1016/j.coldregions.2018.03.003

646   Rignot, E., & Mouginot, J. (2012). Ice flow in Greenland for the International Polar Year 2008-

647   2009: ICE FLOW GREENLAND 2009. *Geophysical Research Letters*, *39*(11), n/a-n/a.

648   https://doi.org/10.1029/2012GL051634

649   Rignot, E., Xu, Y., Menemenlis, D., Mouginot, J., Scheuchl, B., Li, X., et al. (2016). Modeling

650   of ocean-induced ice melt rates of five west Greenland glaciers over the past two

651   decades. *Geophysical Research Letters*, *43*(12), 2016GL068784.

652   https://doi.org/10.1002/2016GL068784

653   Strozzi, T., Werner, C., Wiesmann, A., & Wegmuller, U. (2012). Topography Mapping With a

654   Portable Real-Aperture Radar Interferometer. *IEEE Geoscience and Remote Sensing*

655   *Letters*, *9*(2), 277–281. https://doi.org/10.1109/LGRS.2011.2166751

656   Todd, J., & Christoffersen, P. (2014). Are seasonal calving dynamics forced by buttressing from

657   ice mélange or undercutting by melting? Outcomes from full-Stokes simulations of Store

658   Glacier, West Greenland. *The Cryosphere*, *8*(6), 2353–2365. https://doi.org/10.5194/tc-8-

659   2353-2014

660   Todd, Joe, Christoffersen, P., Zwinger, T., Råback, P., Chauché, N., Benn, D., et al. (2018). A

661   Full-Stokes 3D Calving Model applied to a large Greenlandic Glacier. *Journal of*

662   *Geophysical Research: Earth Surface*, 2017JF004349.

663   https://doi.org/10.1002/2017JF004349

664   Todd, Joe, Christoffersen, P., Zwinger, T., Råback, P., & Benn, D. I. (2019). Sensitivity of a

665   calving glacier to ice–ocean interactions under climate change: new insights from a 3-D

666   full-Stokes model. *The Cryosphere*, *13*(6), 1681–1694. https://doi.org/10.5194/tc-13-

667   1681-2019

668 Vallot, D., Adinugroho, S., Strand, R., How, P., Pettersson, R., Benn, D. I., & Hulton, N. R. J.

669   (2019). Automatic detection of calving events from time-lapse imagery at Tunabreen,

670   Svalbard. *Geoscientific Instrumentation, Methods and Data Systems*, *8*(1), 113–127.

671   https://doi.org/10.5194/gi-8-113-2019

672 van Wessem, J. M., Berg, W. J. van de, Noël, B. P. Y., Meijgaard, E. van, Amory, C., Birnbaum,

673   G., et al. (2018). Modelling the climate and surface mass balance of polar ice sheets using

674   RACMO2 – Part 2: Antarctica (1979–2016). *The Cryosphere*, *12*(4), 1479–1498.

675   https://doi.org/10.5194/tc-12-1479-2018

676 Voytenko, D., Dixon, T. H., Holland, D. M., Cassotto, R., Howat, I. M., Fahnestock, M. A., et al.

677   (2017). Acquisition of a 3 min, two-dimensional glacier velocity field with terrestrial

678   radar interferometry. *Journal of Glaciology*, *63*(240), 629–636.

679   https://doi.org/10.1017/jog.2017.28

680 Werner, C., Strozzi, T., Wiesmann, A., & Wegmuller, U. (2008). A Real-Aperture Radar for

681   Ground-Based Differential Interferometry. In *IGARSS 2008 - 2008 IEEE International*

682   *Geoscience and Remote Sensing Symposium* (Vol. 3, pp. III-210-III–213).

683   https://doi.org/10.1109/IGARSS.2008.4779320

684 Xie, S., Dixon, T. H., Holland, D. M., Voytenko, D., & Vaňková, I. (2019). Rapid iceberg

685   calving following removal of tightly packed pro-glacial mélange. *Nature*

686   *Communications*, *10*(1), 3250. https://doi.org/10.1038/s41467-019-10908-4

687 Xu, Y., Rignot, E., Fenty, I., Menemenlis, D., & Flexas, M. M. (2013). Subaqueous melting of

688   Store Glacier, west Greenland from three-dimensional, high-resolution numerical

689   modeling and ocean observations: SUBAQUEOUS MELTING OF STORE GLACIER.

690   *Geophysical Research Letters*, *40*(17), 4648–4653. https://doi.org/10.1002/grl.50825

691